CrossMark

Facile and Green Preparation of Three-Dimensionally Nanoporous Copper Films by Low-Current Electrical Field-Induced Assembly of Copper Nanoparticles for Lithium-Ion Battery Applications

Lehao Liu, Meicheng Li, Jing Lyu, Tingkai Zhao, and Tiehu Li

Porous copper (Cu) films were facilely and greenly fabricated by low-current electrical field-induced assembly of ∼ 3 nm Cu nanoparticles (NPs) in several minutes using generated hydrogen bubbles as dynamic negative templates. The porous films had open three-dimensionally (3D) interconnected nanopores and uniform pore size distribution and exhibited a hierarchical structure composed of supraparticles that were further composed of the Cu NPs. Lattice-to-lattice connectivity in the self-assembly of the NPs in the 3D structures enables fast charge transport. The structure/morphology of the porous Cu materials can be tuned by adjusting the concentration of the additives, applied potential/current densities and assembly time. A growth mechanism of the porous films was reasonably proposed for the field-induced assembly of the Cu NPs. The porous Cu film-supported Si electrode showed high capacity of 1173 mAh g^{-1} and retention rate of 87% after 10 cycles at 1 C. Our research sheds a light on preparing 3D nanoporous structures especially for suitable electrodes in electrochemical energy storage devices.

1. Introduction

Porous metal materials with abundant pores have many unusual characteristics (e.g., low density and high surface area) different from their solid counterparts (Ref 1, 2). Porous metal materials can work as both light-weight and high-strength structural materials and multi-functional materials for heat dissipation, electromagnetic shielding, shock damping, acoustic absorption, electron transport, catalysis, etc. (Ref 3-6). Particularly, porous copper (Cu) materials have attracted much more attention in the fields of catalysis, separation, sensor and energy conversion and storage, thanks to their comprehensive merits of low cost, high ductility, corrosion resistance, electrochemical stability, and electrical and thermal conductivity, etc. (Ref 7-9).

There are some typical methods for fabricating porous Cu materials, such as casting, powder metallurgy, dealloying and electrodeposition. The structural/morphological features of the porous Cu materials (e.g., pore size, porosity and thickness) mainly depend on the preparation methods and can be tuned to a certain extent by changing the preparation conditions (Ref 10, 11). However, we can clearly summarize the merits and disadvantages of these preparation methods and their resulting porous structures. Casting is a proper method for preparing porous Cu materials with high mechanical strength because of the low porosity (< 60%). But this method has a few drawbacks, such as high energy consumption resulted from the high melting temperature of 1200-1300 °C, much fabrication time, and large pore size (in several hundred μm) (Ref 1, 12-14). Porous Cu materials with 50-85% porosity can be obtained by powder metallurgy; however, the pore size is large (53-1500 μm) and this method needs high compaction pressure (75-300 MPa) and sintering temperature (800-1000 °C) (Ref 9, 15, 16). Dealloying is an important method for preparing porous Cu materials with small pore size (in several hundred nm) and certain thickness, but this technology is restrained by the high pollution caused by the immoderate use of corrosive chemicals and inevitable contamination with other compositions (Ref 17-19). Electrodeposition is a simple method for preparing three-dimensionally (3D) porous Cu films with high porosity (80-99%) based on the Cu deposition in electrical field by using Cu^{2+} ions and gas bubbles as Cu sources and dynamic negative templates, respectively (Ref 20-22). Nevertheless, the pore size and thickness of the electrodeposited porous Cu films are usually at least tens of micrometers, and the distribution of the pore size in the cross-sectional direction is not uniform (Ref 22-26). These morphological characteristics are adverse to increasing surface area and

Lehao Liu, State Key Laboratory of Alternate Electrical Power System with Renewable Energy Sources, North China Electric Power University, Beijing 102206, People's Republic of China; School of Materials Science and Engineering, Northwestern Polytechnical University, Xi'an 710072, People's Republic of China; and Department of Chemical Engineering, University of Michigan, Ann Arbor, MI 48109; Meicheng Li, State Key Laboratory of Alternate Electrical Power System with Renewable Energy Sources, North China Electric Power University, Beijing 102206, People's Republic of China; Jing Lyu, School of Materials Science and Engineering, Northwestern Polytechnical University, Xi'an 710072, People's Republic of China; and Department of Chemical Engineering, University of Michigan, Ann Arbor, MI 48109; and Tingkai Zhao and Tiehu Li, School of Materials Science and Engineering, Northwestern Polytechnical University, Xi'an 710072, People's Republic of China. Contact e-mails: liulehao@yahoo.com and mcli@ncepu.edu.cn.

facilitating electron/ion and fluid transport as required for the applications in sensor, catalysis, lithium-ion battery (LIB), etc. (Ref [20], [27-30]). Therefore, facile and green preparation methods for 3D nanoporous Cu films with uniform pore size distribution throughout the films are still much desired.

In this work, we develop a facile and green way to fabricate 3D nanoporous Cu films by electrical field-induced assembly of Cu nanoparticles (NPs). Compared to the aforementioned methods, this preparation route exhibits a few obvious advantages: (1) low current density and energy depletion due to the obviation of the reduction reaction from Cu^{2+} ions to Cu^0 crystal; (2) short preparation time in several minutes; and (3) avoidance of subsequent template removal process by using H_2 bubbles as dynamic templates. More importantly, the 3D porous Cu films have nanosized pores and uniform pore size distribution, mainly owing to the use of ultra-small Cu NPs ($\sim$ 3 nm) as building blocks/units. We have also investigated the effects of the preparation conditions (e.g., additives, potential/current densities and assembly time) on the porous films and proposed a growth mechanism for the fabrication of the porous Cu films that could be applied to field-induced assembly of other NPs for porous materials. In addition, the 3D nanoporous Cu films can serve as ideal substrates for active electrode materials to widen their applications in lithium-ion batteries.

2. Experimental

2.1 Materials and Chemicals

Copper dichloride dihydrate ($CuCl_2 \cdot 2H_2O$), cetyltrimethylammonium bromide (CTAB), L-ascorbic acid, acetone, acetic acid and sulfuric acid were purchased from Sigma-Aldrich. Deionized water was obtained from a Barnstead E-pure water purification system. Si nanopowders were purchased from Alfa Aesar.

2.2 Synthesis of Stable Cu NP Aqueous Solutions

The synthesis procedure is described in our previous paper (Ref [31]). Specifically, 25 mL of 0.06 M $CuCl_2$ and 0.01 M CTAB aqueous solution and 25 mL of 0.8 M L-ascorbic acid and 0.01 M CTAB aqueous solution were first prepared with the assistance of ultrasonication and stirring. After that they were mixed and then heated at 45 °C for 42 h under violent magnetic stirring. The mixed solution containing 0.4 M L-ascorbic acid, 0.03 M $CuCl_2$ and 0.01 M CTAB turned from green/light brown to red, which indicated the generation of Cu NPs. The pure Cu NP aqueous dispersions were obtained after centrifugation at 10,000 rpm for 3 times and dialysis for 1 h using a dialysis membrane to remove excessive $CuCl_2$, CTAB and L-ascorbic acid. The size and shape of the Cu NPs were controlled by changing reaction time and the concentrations of the raw materials.

2.3 Fabrication of 3D Nanoporous Cu Films and Cu/Si Composites by Electrical Field-Induced Assembly of the Cu and Si NPs

Cu foils were firstly cleaned with dilute HCl solution (7.4 wt.%), acetone, and deionized water, respectively. Porous Cu films were prepared by using an Epsilon electrochemical workstation (Bioanalytical Systems, Inc.) with a Pt wire and a Cu foil as anode and cathode, respectively. The distance between the two parallel electrodes was $\sim$ 1 cm. The Cu NP solutions added with different amount of acetic acid and CTAB were used as electrolytes. A chronoamperometry (CA) method was applied under various potential/current and time for the assembly of the Cu NPs on the Cu foils. All the samples were washed with ethanol and water sequentially and were then dried under vacuum at 60 °C for 12 h. Porous Cu/Si composite films with $\sim$ 0.25 mg cm^{-2} Si mass loading were prepared by electrodepositing Si NPs in the porous Cu film electrodes in a 5 wt.% polydopamine-decorated Si NP aqueous solution at 2000 mV for 15 min.

2.4 Characterizations

Transmission electron microscope (TEM) images were taken by a JEOL 3011. The TEM specimens of the Cu NPs were prepared by dripping a single drop of the Cu NP aqueous solution onto a carbon-coated Au grid and then allowing the drop to dry in air. The average size and zeta potential of the Cu NPs were measured by dynamic light scattering (DLS) (Zetasizer Nano-ZS, Malvern Instruments, U.K.). The porous Cu films were scraped from the Cu electrodes and then dispersed in deionized water under an ultrasonication treatment for 10 s for TEM characterization. Scanning electron microscope (SEM) images were obtained by a FEI Nova 200 SEM. For electrochemical measurements of the porous Cu/Si composites as anodes in lithium-ion batteries, two-electrode CR2032 coin cells were assembled in a glove box filled with argon (oxygen content: < 3 ppm; moisture content: < 3 ppm) with a Celgard 2400 separator from MTI Corporation. A Li foil and a porous Cu/Si composite film (1 cm × 1 cm) were used as counter/reference electrode and working electrode, respectively. 1 M lithium hexafluorophosphate in a solution of 1:1 volume ratio of ethylene carbonate and dimethyl carbonate was used as electrolyte. The charge and discharge cycling was conducted using a Maccor Series 4000 48-channel battery tester (Maccor, USA) in a potential range of 0.01-1.2 V (versus Li/Li$^+$) at various C rates (1 C = 4000 mA g^{-1}). Electrochemical impedance spectra were obtained using a CHI660D electrochemical workstation (CH Instrument Inc.) by applying a sine wave with amplitude of 5 mV over a frequency range from 100 K to 0.01 Hz.

3. Results and Discussion

Developing suitable Cu NPs as building blocks/units is one of the most essential steps in the successful assembly for porous Cu films. Most of the synthesis of Cu NPs in liquid phase involves the use of strong reductants [e.g., hydrazine (Ref [32], [33]), sodium borohydride (Ref [34], [35]) and sodium hypophosphite (Ref [36])]. To impede the oxidation of the Cu NPs, the reaction process needs to carefully handled in inert gases, and a few organic solvents [e.g., ethylene glycol (Ref [37]), dimethylether (Ref [38], [39]) and tetrahydrofuran (Ref [38], [39])] are usually used as protective mediums. Moreover, silica (Ref [40]) and different organic ligands, such as CTAB (Ref [32], [41]), polyvinylpyrrolidone (PVP) (Ref [42], [43]) and polyallylamine (PAAM) (Ref [44], [45]), are coated on the Cu NPs to hinder their oxidation and agglomeration. Albeit the great progress in the preparation of Cu NPs, stable Cu NP aqueous dispersions still present considerable chemical challenges (Ref [44], [46-51]). The

Cu NPs in solvents more intend to aggregate than NPs from other metals, for instance well-known Au colloids, because of the lower surface charges (Ref 46, 48, 52). The Cu NPs are also more chemically active than Au and Ag NPs, which leads them to be more easily oxidized, especially in water (Ref 46, 53, 54).

Ideal Cu NP dispersions should be (1) colloidally stable against oxidation and agglomeration within the time-frame adequate for the fabrication of porous Cu films, and (2) capable of self-assembly in aqueous mediums. A suitable synthetic route has been developed in our previous study (Ref 31). Briefly, we obtained ∼ 3 nm Cu NP aqueous dispersions by heating a solution of Cu salt in the presence of L-ascorbic acid and CTAB at 45 °C for 42 h under vigorous stirring. It is also a green method because of the use of L-ascorbic acid and water as mild reductant and solvent, respectively, as well as the preparation in ambient atmosphere without the protection of inert gases. The combination of CTAB offers positive surface charge for stabilizing the Cu NPs, while L-ascorbic acid prevents the oxidation of the Cu NPs. The long hydrocarbon chain in CTAB could impede interparticle electron transport; however, we can take advantage of the lability nature of the surface ligand in the self-assembly process for high-conductivity porous films.

The as-synthesized Cu NPs were discrete with a relatively narrow size distribution (Fig. 1A). An average diameter was calculated to be of 3.0 ± 0.56 nm by counting all the NPs in the TEM image (Fig. 1B). DLS technology gave an average size of 10.6 nm, which is bigger than the TEM size ascribed to the presence of a coating layer from bound CTAB and water molecules (inset of Fig. 1A). Higher-resolution TEM image
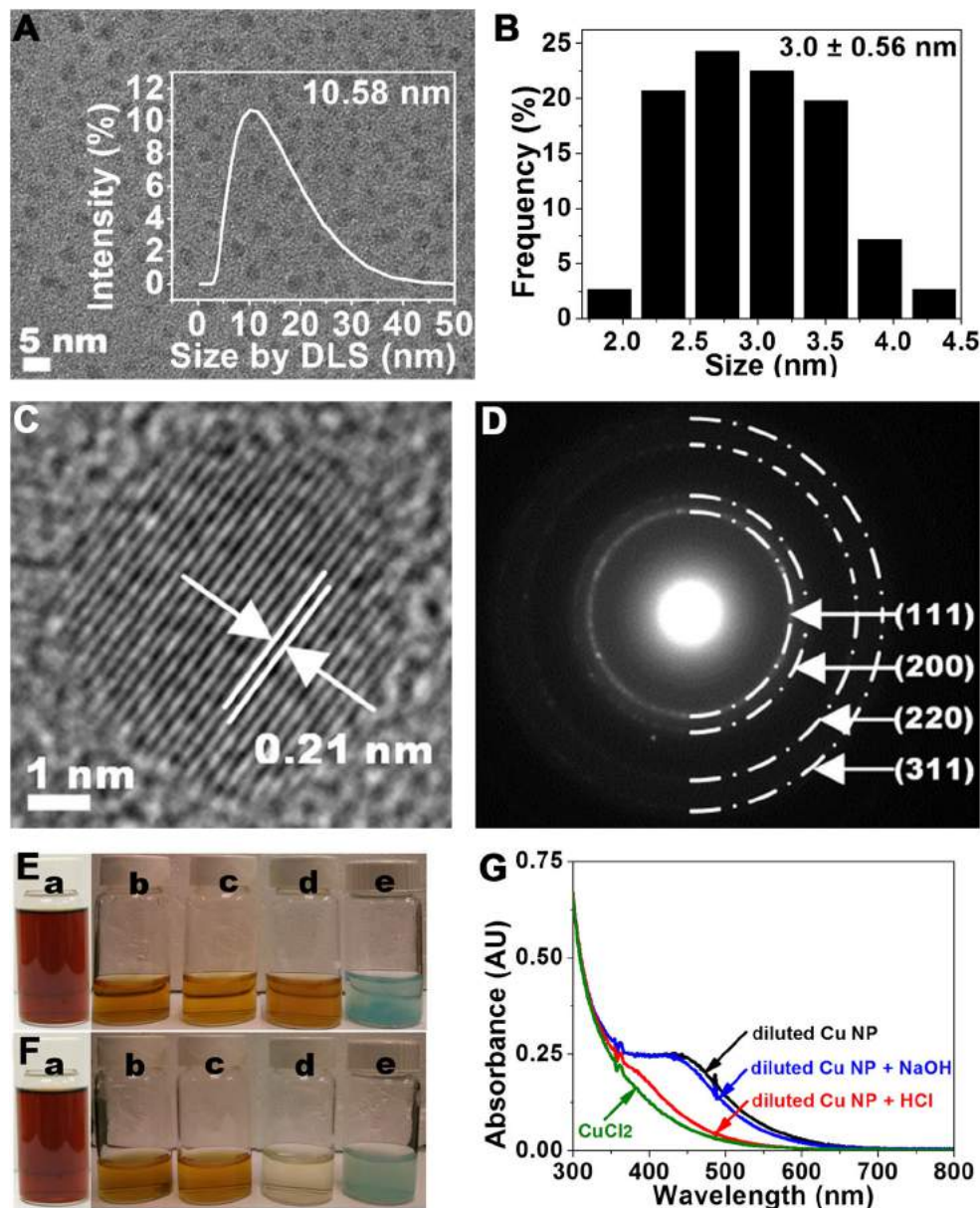

Fig. 1 (A) TEM image and (B) corresponding size distribution histogram of the Cu NPs. (C) HR-TEM image of a Cu NP and (D) the selected area electron diffraction pattern of the Cu NPs. Optical photographs of the (*a*) original Cu NP solution, diluted Cu NP solutions with one-tenth of the original Cu concentration after dripping (*b*) 0 and 0.5 mL 0.1 M (*c*) NaOH and (*d*) HCl solutions, and (*e*) 0.03 M CuCl₂ solution after dripping 0.5 mL 0.1 M NaOH solution, after (E) 1 h and (F) 1 month of storage under ambient atmosphere, and (G) their corresponding UV–Vis absorbance spectra. The inset in (A) shows a corresponding size distribution graph obtained by dynamic light scattering
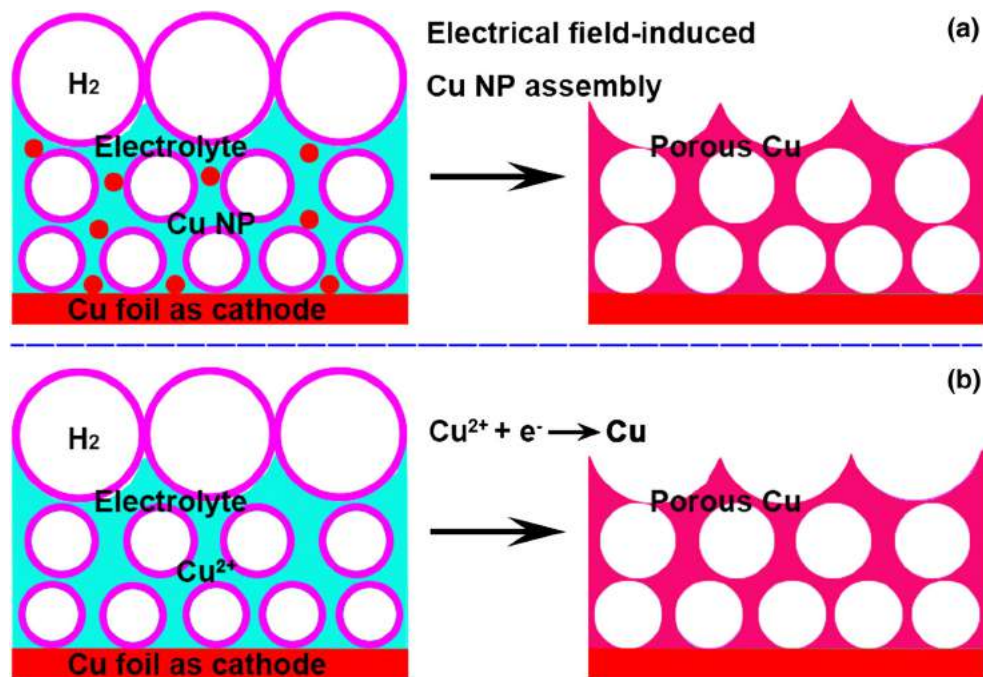
Fig. 2 Schematic presentations of the preparations of porous Cu materials in electrical field by using (a) Cu NPs and (b) Cu^{2+} ions as Cu sources, respectively

showed the lattice distance of the inorganic core of the NPs to be 0.21 nm (Fig. 1C) corresponding very well to the spacing of (111) lattice planes in the face-centered cubic (FCC) Cu crystal. The selected area electron diffraction (SAED) pattern further manifested that the first, second, third and fourth diffraction rings (from center to outside) corresponded to the lattice distances of 0.21, 0.18, 0.13 and 0.11 nm, respectively (Fig. 1D). This sequence is well consistent with the lattice planes of (111), (200), (220) and (311) metallic FCC Cu. Cumulatively these findings proved that the synthesized NPs were made from metallic Cu rather than from copper oxide(s).

We also observed the stability of the Cu NP aqueous dispersions by optical photography (Fig. 1E and F). The original and diluted Cu NP aqueous dispersions were red and yellow-orange, respectively, and displayed no indication of sedimentation or oxidation after 1 month of storage under ambient atmosphere condition (Fig. 1E and F, a-b). After adding NaOH solution into $CuCl_2$ solution, a lot of flocculates generated and the solution became less transparent due to the formation of $Cu(OH)_2$ (Fig. 1E and F, e). On the contrary, the diluted Cu NP dispersion with the injection of NaOH still maintained the same color and no sediment was observed (Fig. 1E and F, c), which further indicated the high stability and dispersity of the Cu NPs in water. This should be attributed to the synergistic effect of L-ascorbic acid and CTAB, which formed stabilized coating shells on the surfaces of the Cu NPs, thus, effectively preventing the oxidation and aggregation of the Cu NPs (Ref 42, 47, 55). Moreover, the diluted Cu NP dispersion changed from yellow-orange to colorless after the addition of HCl (Fig. 1E and F, d), which should be ascribed to the higher chemical activity of nanoscaled Cu than bulk Cu. The UV–Vis absorbance spectra were further taken to investigate the stability of the Cu NPs in water (Fig. 1G). The Cu NP dispersion showed a broad surface plasmon peak at ∼ 440 nm, indicating the existence of ultra-small Cu NPs with the size of < 4 nm that was consistent with Fig. 1(A), (B) and (C) (Ref 31, 55-58). When adding NaOH solution into the NP dispersion, the position and shape of the absorbance peak remained almost unchanged, indicating the high stability of the Cu NPs that agreed with Fig. 1(E) and (F). However, when adding HCl solution into the NP dispersion, the absorbance peak of the Cu NPs disappeared behaving more like that of the $CuCl_2$ solution, which further confirmed the high chemical activity of the Cu NPs that was consisted with Fig. 4(e) and (f). In short, we prepared Cu NP aqueous dispersions with high stability against agglomeration and oxidation, and we predicated the NP dispersions can afford the self-assembly process for porous Cu films.

In the traditional electrodeposition process, two fundamental reactions occur on the cathode: (1) $2H^+ + e^- \rightarrow H_2$ (g); and (2) $Cu^{2+} + 2e^- \rightarrow Cu$ (s). Consequently, a porous Cu film forms on the cathode with the generated H_2 bubbles as dynamic negative templates (Fig. 2b). As well, another porous Cu film can grow on the cathode due to the movement and deposition of the Cu NPs with the assistance of Coulombic force by using H_2 bubbles as dynamic negative templates (Fig. 2a). The self-assembly process of the NPs and the structure/morphology of the resulted porous Cu film can be controlled by adjusting the concentration of the additives (i.e., acetic acid and CTAB) in the electrolyte, applied potential/current densities and self-assembly time.

We first studied the effect of the additives on the growth of porous Cu films. Acetic acid has the ability to prevent the coalescence and growth of H_2 bubbles and stabilize the gas templates (Ref 23, 59). When acetic acid was not added into the electrolyte, dendritic structures interconnected to form a porous Cu film (Fig. 3a), but the film was not completely covered on the electrode surface, which was attributed to the generation of much H_2 and coalescence of the H_2 bubbles into instable and big bubbles that made the Cu NPs unstably assemble on the bubble templates. High-magnification SEM images revealed that the average pore size of the porous Cu
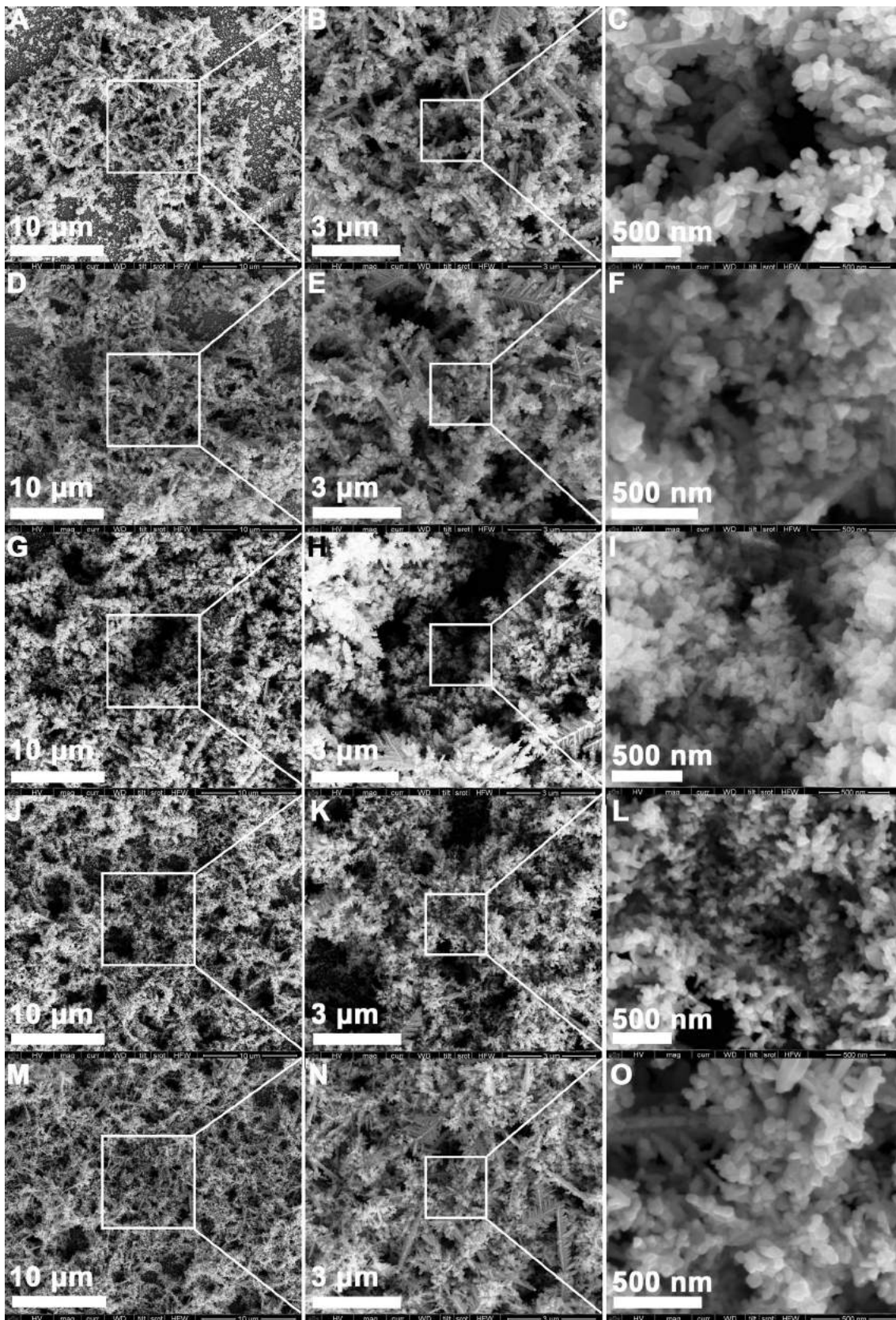
Fig. 3 SEM images of porous Cu films fabricated by electrical field-induced assembly of the Cu NPs in electrolytes added with (a-c) 0, (d-f) 0.1, (g-i) 0.4 and (j-l) 0.8 M acetic acid but without CTAB, and (m-o) 0.4 M acetic acid and 2 mM CTAB at potential/current densities of 800 mV/51 mA cm^{-2} for 10 min, respectively
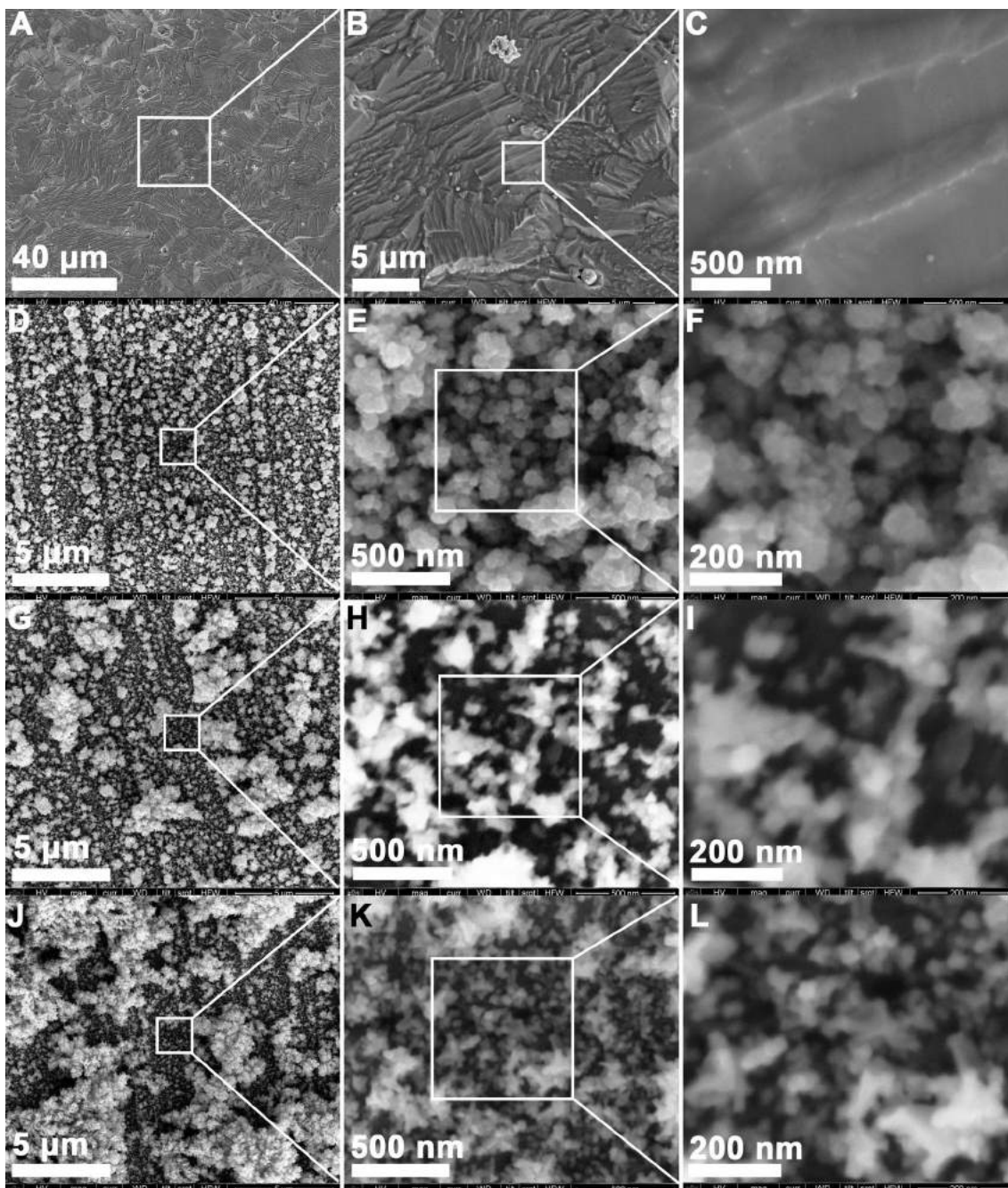
Fig. 4 SEM images of porous Cu films fabricated on pretreated Cu foil electrodes (a-c) by electrical field-induced assembly of 0.03 M Cu NPs in electrolytes added with 0.4 M acetic acid and 2 mM CTAB at various potential/current densities of (d-f) 5/13, (g-i) 10/27, (j-l) 100/42 mV/ mA cm^{-2} for 8 min, respectively

film was 450 nm (Fig. 3b), and the dendrites were constituted with agglomerates/aggregates (or clusters) of ~ 70 nm (Fig. 3c). When the concentration of acetic acid increased to 0.1 M, the H$_2$ bubbles became more stable and smaller and the Cu NPs assembled into a 3D porous film with an average micropore size of 3.5 μm completely covered on the electrode (Fig. 3d). The dendritic structures also formed smaller nanopores of ~ 410 nm in size (Fig. 3e) and were composed of ~ 55 nm agglomerates (Fig. 3f). When the concentration of acetic acid increased to 0.4 M, the 3D porous Cu film was still fully covered on the electrode with an average micropore size of 1.8 μm and an average agglomerate size of 50 nm

(Fig. 3g, h and i). When increasing the concentration of acetic acid to 0.8 M, the pore size distribution became more uniform, and the agglomerates interconnected to form ~ 55 nm pores (Fig. 3j, k and l). As a common cationic surfactant, CTAB is also capable of diminishing the surface tension of the H$_2$ bubbles and stabilizing the gas templates (Ref 24, 60). Compared to the porous film prepared without CTAB (Fig. 3g, h and i), the porous Cu film prepared with CTAB-involved electrolyte showed much more uniform pore size distribution with smaller micropore and nanopore sizes of ~ 1.0 μm and ~ 250 nm, respectively, and smaller agglomerate size of ~ 40 nm (Fig. 3m, n and o).
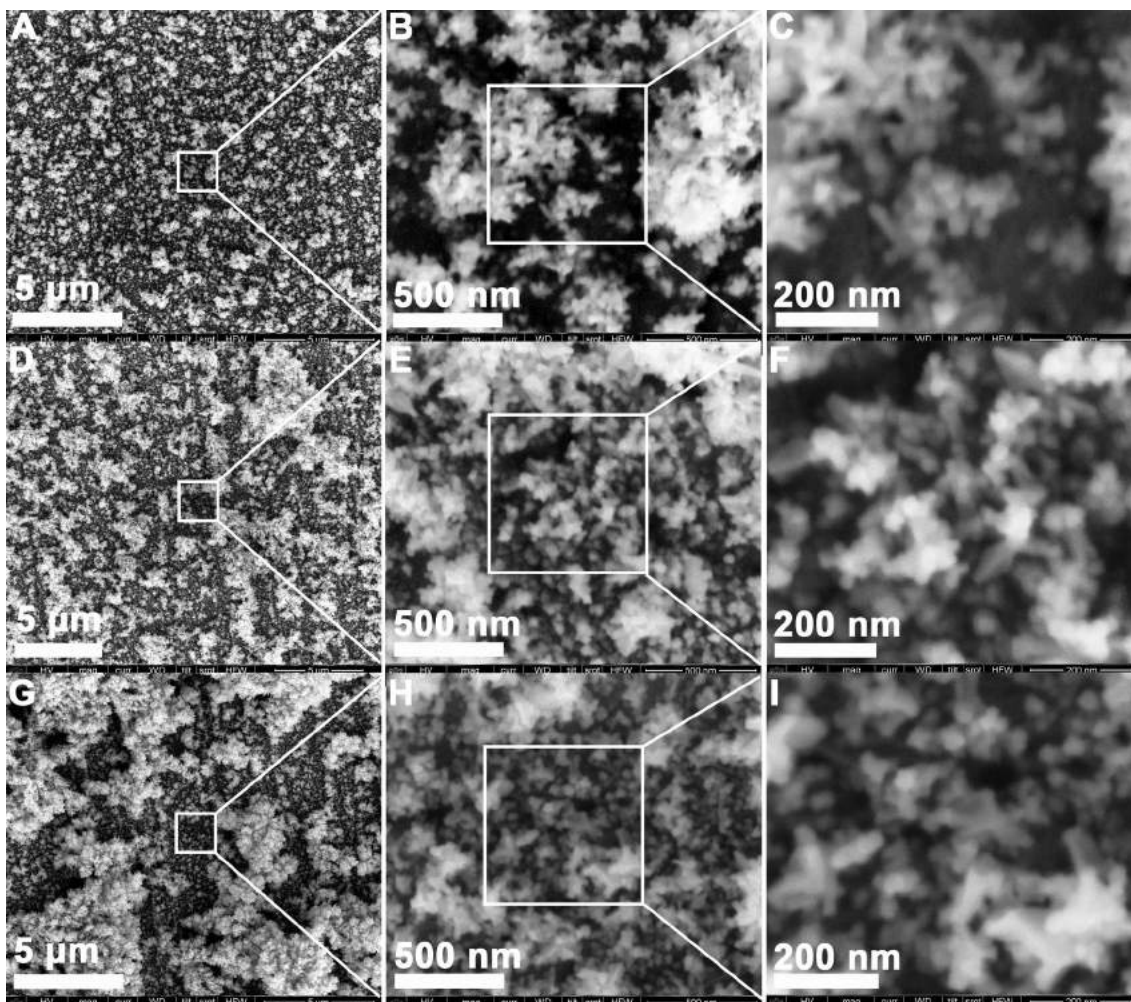
Fig. 5 SEM images of porous Cu films fabricated by electrical field-induced assembly of 0.03 M Cu NPs in electrolytes added with 0.4 M acetic acid and 2 mM CTAB at potential/current densities of 100 mV/42 mA cm^{-2} for (a-c) 2, (d-f) 4 and (g-i) 8 min, respectively

Adjusting the applied potential/current densities can not only change the formation rate of H$_2$ and the coalescence of the gas bubbles but also determine the strength of the Coulombic force, thus affecting the self-assembly behaviors of the Cu NPs on the gas templates and the growth of the porous Cu film. The pretreated Cu foil electrode was relatively flat but with many microsized valleys (Fig. 4a, b and c). However, after 8 min self-assembly of the Cu NPs at 5 mV/13 mA cm^{-2}, many isolated islands with an average size of 250 nm formed on the electrode (Fig. 4d). High-magnification SEM images further disclosed that the islands were constituted with ~ 30 nm agglomerates (Fig. 4e and f). When increasing the potential/current densities to 10 mV/27 mA cm^{-2}, the average size of the islands increased to ~ 1.0 μm (Fig. 4g). Actually, the dendrites with an average length of 180 nm connected each other to form a 3D porous structure with an average pore size of 150 nm (Fig. 4h and i). When increasing the potential/current densities to 100 mV/42 mA cm^{-2}, the generation rate of H$_2$ increased and the gas bubbles were forced to leave from the electrode surface, and thereby inhibited the coalescence and growth of the gas bubbles. Meanwhile, the Cu NPs moved rapidly toward the cathode under the strong electrical field and self-assembled on the smaller gas templates, and therefore resulted in the increase of the size and interconnection of the

islands and more coverage of the dendritic structures on the electrode surface (Fig. 4j). Moreover, the average length of the dendrites and the average pore size decreased to 100 nm and 50 nm, respectively (Fig. 4k and l).

Self-assembly time also had important effect on the growth of porous Cu films. After 2 min at 100 mV/42 mA cm^{-2}, the Cu NPs assembled into islands with an average size of 300 nm (Fig. 5a), and these islands connected to form an incontinuous porous dendritic structure composed of ~ 30 nm agglomerates (Fig. 5b and c). When increasing to 4 min, more Cu NPs assembled on the electrode surface. As a result, the average sizes of the islands and dendrites increased to 1.5 μm and 90 nm, respectively (Fig. 5d and e). But the average size of the pores resulted from the interconnection of the dendrites maintained to be 50 nm (Fig. 5f). When increasing to 8 min, the islands further growed and interconnected and were almost completely covered on the electrode surface (Fig. 5g). It should be noted that adjusting the time does not change the generation rate of H$_2$ and the Coulombic force and assembly rate of the Cu NPs. So the average sizes of the agglomerates and pores were almost not affected by the self-assembly time (Fig. 5h and i).

With the above-mentioned discussions in mind, we started the preparation of 3D porous Cu films at high potential/current densities of 2000 mV/75 mA cm^{-2} for different time. When
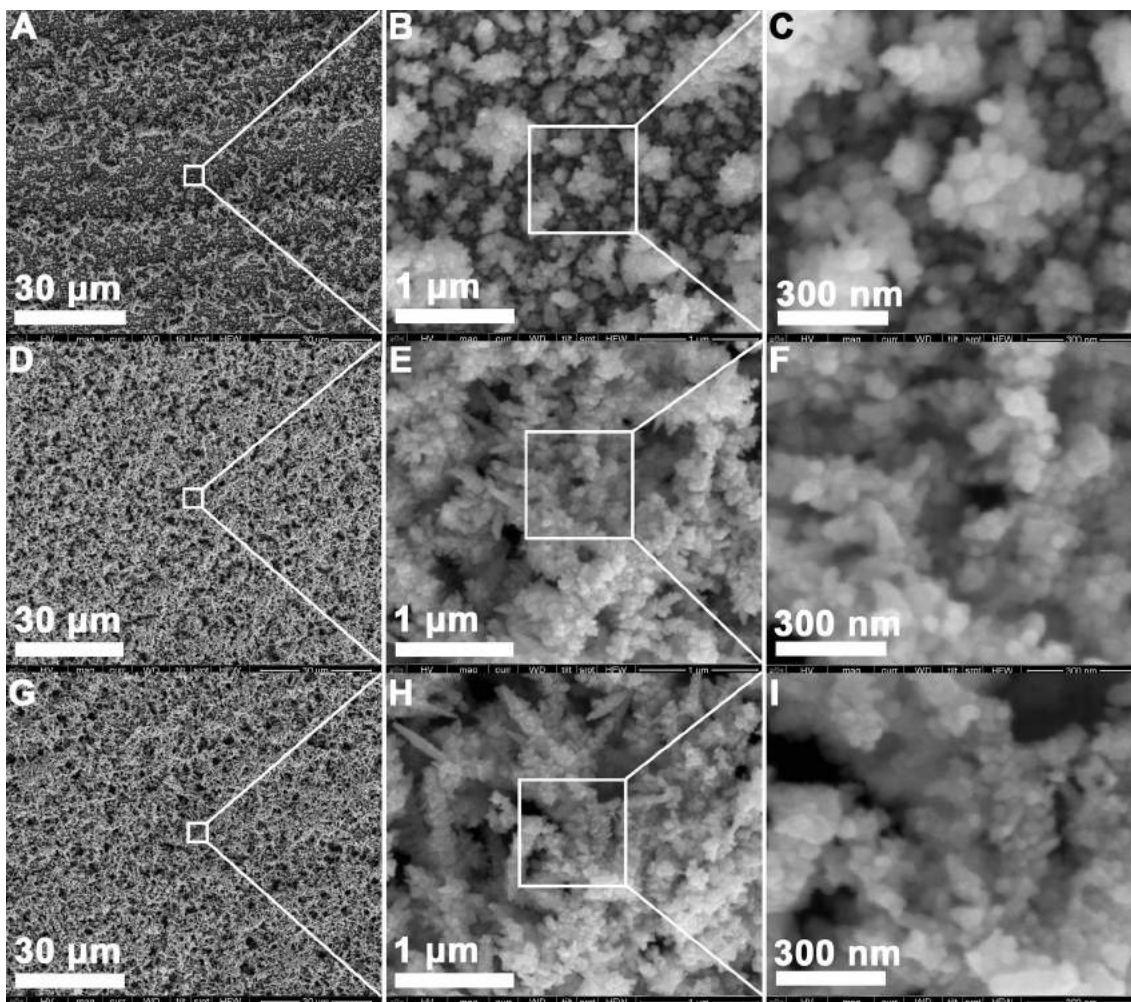
Fig. 6 SEM images of porous Cu films fabricated by electrical field-induced assembly of 0.03 M Cu NPs in electrolytes added with 0.4 M acetic acid and 2 mM CTAB at potential/current densities of 2000 mV/75 mA cm^{-2} for (a-c) 6, (d-f) 8 and (g-i) 10 min, respectively

the self-assembly time was too short (6 min), the Cu NPs formed discrete dendrites and islands with average sizes of 4.5 μm and 90 nm, respectively (Fig. 6a). The dendrites and islands were also composed of agglomerates with an average size of 40 nm (Fig. 6b and c). When increasing the assembly time to 8 min, more Cu NPs assembled into a 3D porous Cu film with uniform pore size distribution, and the average and maximum pore sizes were 200 nm and < 5.0 μm, respectively (Fig. 6d and e). The dendritic structures were also composed of ~ 40 nm agglomerates (Fig. 6f). The area density of the 3D porous Cu film was ~ 0.40 mg cm^{-2} by weighing the completely scraped Cu film from the electrode surface. Owing to the low mass loading of the porous Cu film, we did not measure the surface area easily by using the Brunauer–Emmett–Teller (BET) technology. But we can conveniently count the number of the pores in the SEM images and then estimate the specific surface area (A_s) to be ~ 10.02 m^2 g^{-1} by the equation: $4\pi R_a^2 N_p L/D_a$, where the average pore radius: R_a = 100 nm, the pore number: N_p = 3.19 × 10^{10} cm^{-2}, the 2D shape factor of a pore: L = 1, and the area density: D_a = 0.40 mg cm^{-2}. Notably, this estimated value was theoretically much lower than the veritable value, because it only took the observed pores in account without considering the constitution of the porous film with 40 nm agglomerates and

3 nm NPs. Since the porous film was already entirely covered on the electrode surface, the micromorphology of the porous Cu film showed no distinct change even with the increase in the assembly time to 10 min (Fig. 6g, h and i). Compared to the traditional casting, powder metallurgy and dealloying, this field-induced assembly was simple and environmental friendly and required less energy and time completely comparable to the electrodeposition method.

Lower-magnification SEM images also revealed the uniform surface structure of the 3D porous Cu films (Fig. 7a, b and c), and the thickness of the films was determined to be ~ 7 μm (Fig. 7d). Even inside the films preserved the porous dendritic structure, and the average sizes of the dendrites, pores and agglomerates were 700 nm, 200 nm and 40 nm, respectively, which not only corresponded very well to the surface morphological characteristics but also further exposed the uniformity of the porous Cu films (Fig. 7e and f). It should be mentioned that this porous film structure is quite different from the previous reported porous Cu film structure prepared by electrodeposition, where the pore size varied along the cross-sectional direction due to the deposition of generated Cu crystal only within the interstitial spaces between the H$_2$ bubbles that coalesced and growed bigger perpendicular to the cathode (Ref 22-25, 59). In stark contrast, the obviation of the transformation
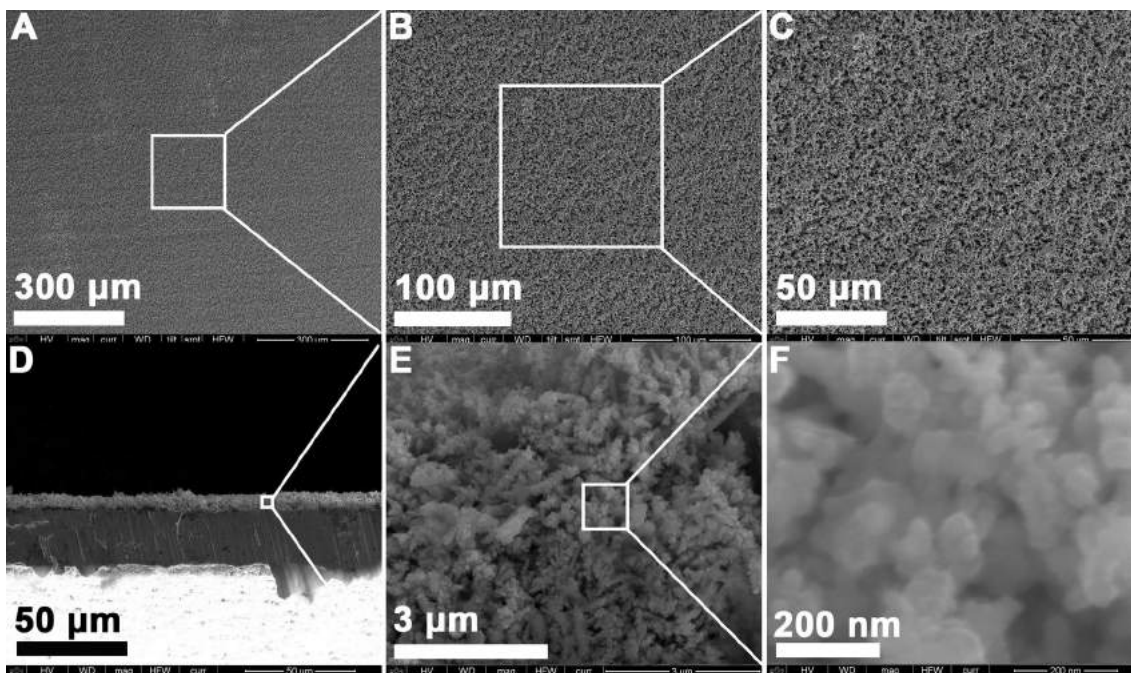
Fig. 7 (a-c) Surficial and (d-f) cross-sectional SEM images of the porous Cu films fabricated by electrical field-induced assembly of 0.03 M Cu NPs in the electrolytes added with 0.4 M acetic acid and 2 mM CTAB at potential/current densities of 2000 mV/75 mA cm^{-2} for 8 min

from Cu^{2+} to Cu^0 crystal by directly using the Cu NPs as Cu sources and rapid movement and deposition of the Cu NPs incompletely on (or in) the H_2 bubbles under long-range Coulombic force resulted in the uniformity of the porous Cu film structure (e.g., the unchanged pore size along the cross-sectional direction). As such, the current requirement was reduced at least by an order of magnitude compared with the standard electrodeposition process (Ref [22-24], [59]).

TEM was further utilized to observe the structure of the 3D porous Cu films. As expected we can see the dendritic structure with branch lengths ranging from several tens of nanometer to several micrometers (Fig. [8]a), which was in accordance with the SEM images (Fig. [6]d, e and f, [7]). Further investigation at higher-resolution manifested that the dendrites were actually a hierarchical structure. The essential constitution unites were NP agglomerates/aggregates (also known as supraparticles) with a size range of 30-50 nm (Fig. [8]b), which agreed with Fig. [6](f) and [7](f). The agglomerates were further composed of interconnected individual NPs with a size range of 2-7 nm, which corresponded very well with the size of the Cu NPs observed in Fig. [1]. In these assemblies we did not observe any interparticle gaps, which would be ascribed to the CTAB coating on the Cu NPs. The insulating organic shells on NPs and related hindered charge transport might have prevented earlier studies of such films for electronics (Ref [61]). On the contrary, we can clearly seen distinct NP-to-NP bridging (Fig. [8]c) with lattice-to-lattice connectivity (Fig. [8]d). This morphological feature is conducive to metallic charge transfer in the fabricated Cu films. As a proof of the conductive nature of the NP-to-NP bridges, the lattice space in the interfacial areas between the NPs was determined to be 0.21 nm (Fig. [8]d), which corresponds very well to the distance between the (111) lattice planes in FCC Cu crystal. The spontaneous formation of NP–NP bridges was previously observed for semiconductor NPs, but it was not observed for metallic particles (Ref [61-63]). This discovery was vital to the

successful integration of NP self-assembly phenomena in technology of electronic devices.

Fortunately, we observed the distribution of the Cu NPs in the porous films by further TEM investigation. Similar to the construction disclosed in the previous SEM and TEM images, the dendrites consisted of agglomerates with an average size of 40 nm (Fig. [9]a). We can also see plenty of NPs on/around the dendrites, and the diameter of the NPs was 1.5-6.0 nm with an average value of 3.2 nm (Fig. [9]b). Higher-resolution TEM further revealed that both the Cu NPs and porous film clearly showed the (111) lattice spacing of 0.21 nm (Fig. [9]c and d). A few NPs got close to the dendrites, but a few NPs had been deposited on the dendrites and interconnected to form the agglomerate structure. Furthermore, we can observe the lattice planes throughout the whole dendrites and the Cu NPs on the dendrites, which is beneficial to electron transport in the Cu films. This further proves that our method by electrical field-induced assembly of NPs can afford preparing high-conductivity metallic films.

Based on the aforesaid discussions, we can assume the growth mechanism of the porous Cu films prepared by electrical field-induced assembly of Cu NPs (Fig. [10]): (1) Cu NPs move toward the cathode in the electrolyte under long-range Coulombic force and meanwhile the gas bubbles generate due to the reduction of H^+ ions; (2) the Cu NPs self-assembled into supraparticles (i.e., NP agglomerates or clusters) on the cathode by using the H_2 bubbles as dynamic negative templates; (3) the supraparticles interconnected into dendrites with many branches; (4) more supraparticles formed on the dendrites to make the dendrites interconnect into the 3D porous structure. This well-organized/ordered self-assembly process eventually resulted in the hierarchical but uniform structure of the 3D porous Cu films (Fig. [6], [7], [8] and [9]).

Si is a promising anode material for next-generation lithium-ion batteries due to its higher theoretic capacity of
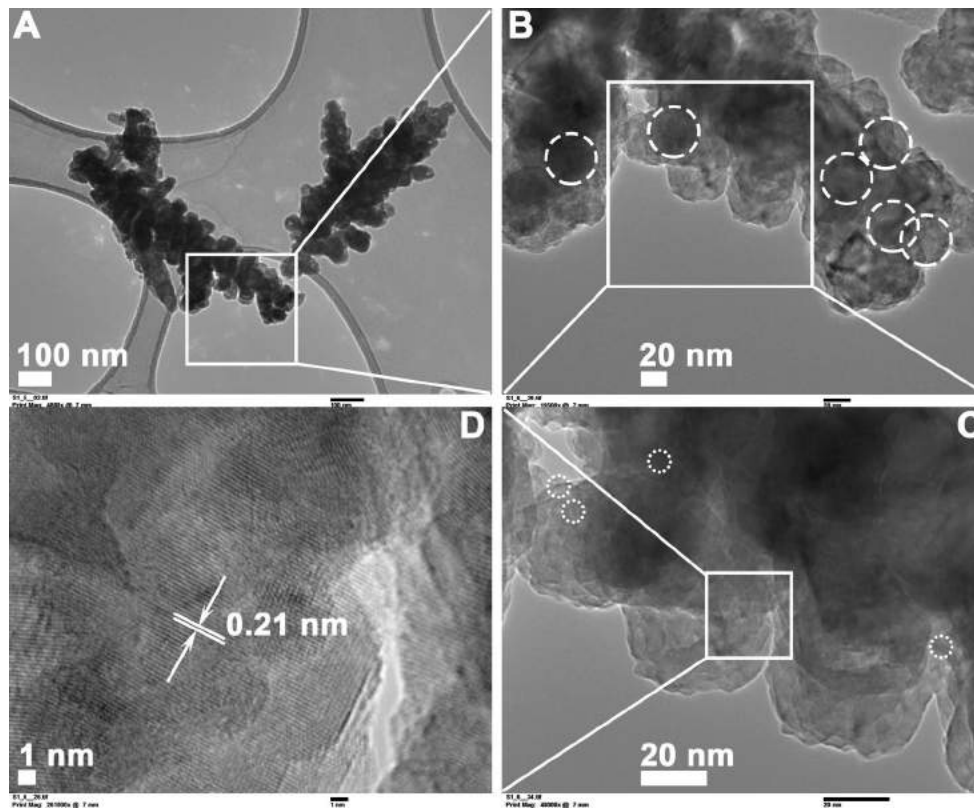
Fig. 8 TEM images of the porous Cu films fabricated by electrical field-induced assembly of 0.03 M Cu NPs in the electrolytes added with 0.4 M acetic acid and 2 mM CTAB at potential/current densities of 2000 mV/75 mA cm^{-2} for 8 min
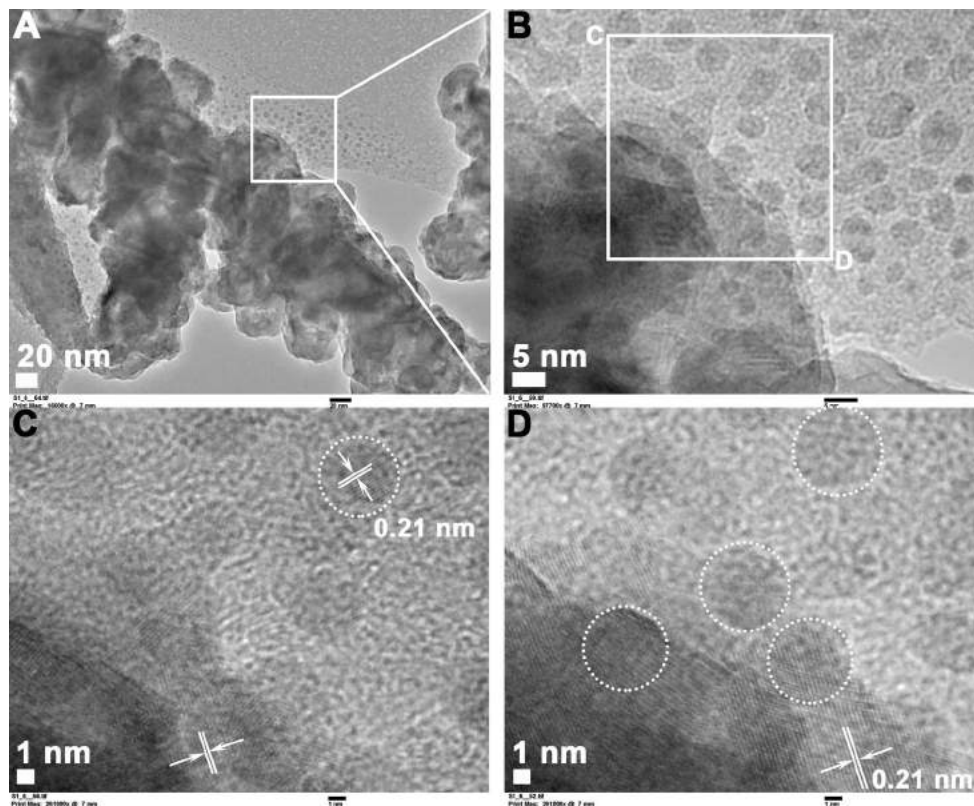

Fig. 9 TEM images of the porous Cu films fabricated by electrical field-induced assembly of 0.03 M Cu NPs in the electrolytes added with 0.4 M acetic acid and 2 mM CTAB at potential/current densities of 2000 mV/75 mA cm^{-2} for 8 min

4200 mAh g^{-1} (Li$_{22}$Si$_5$) than graphite (372 mAh g^{-1}, LiC$_6$), higher work safety, better environmental friendliness and abundance, etc. (Ref 64-68). However, the practical implementation of Si is impeded dramatically by its poor cycling stability (Ref 69, 70), which is caused by its low intrinsic electrical conductivity and huge change in volume change of up to 300-400% in response to full lithiation/delithiation (Ref 71-73). To circumvent these problems, we electrodeposited Si NPs into the pores in the 3D porous Cu films (Fig. 11a, c and d). The Si NPs had a wide si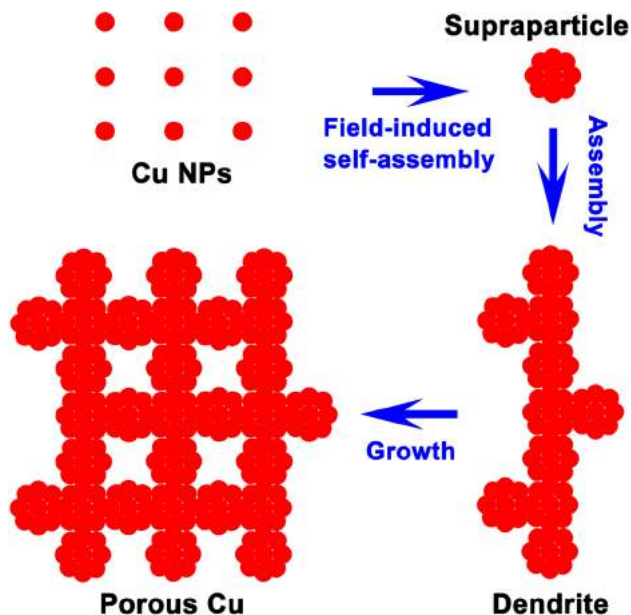ze distribution of 22-480 nm with an average diameter of 123.0 ± 70.2 nm (Fig. 11b). The porous Cu substrates can offer high electronic conductivity and abundant voids to facilitate the charge transfer and meanwhile accommodate the Si volume variation during charge and discharge processes. As a result, the porous Cu/Si composite showed high initial charge and discharge capacities of 1587 and 1958 mAh g^{-1} with a Coulombic efficiency of 81.1% at 0.1 C, respectively (Fig. 11e). The lithiation and delithiation took place at 0.1 and 0.4 V, respectively. The porous Cu/Si electrode also exhibited high capacity of 1173 mAh g^{-1} and capacity retention of 86.5% with a high Coulombic efficiency of 99.7% after 10 cycles at 1 C (Fig. 11f). This capacity value was three times higher than that of the traditional graphite anode ($\sim$ 372 mAh g^{-1} in theory), indicating the excellent electrochemical performance of the porous Cu/Si structure. The resistance of the porous Cu/Si electrode changed from 27 to 32 Ω after 10 cycles with a small increase of 5 Ω, which further verified the high structural and electrical stability of the porous Cu/Si composite electrode due to the robust hierarchical nanostructure (Fig. 11g).

4. Conclusions

Well-dispersed $\sim$ 3 nm Cu NPs were prepared in aqueous media, and their extremely high stability in ambient atmosphere enabled us to fabricate 3D porous Cu films by electrical field-induced assembly by using H$_2$ bubbles as dynamic negative templates. This self-assembly method was simple and green and required less energy and time, compared to the casting, powder metallurgy and dealloying. Importantly, the porous films had open 3D interconnected nanopores and uniform pore size distribution, compared to the electrodeposited films. The porous Cu films also showed a hierarchical structure composed of supraparticles that were further composed of the Cu NPs.
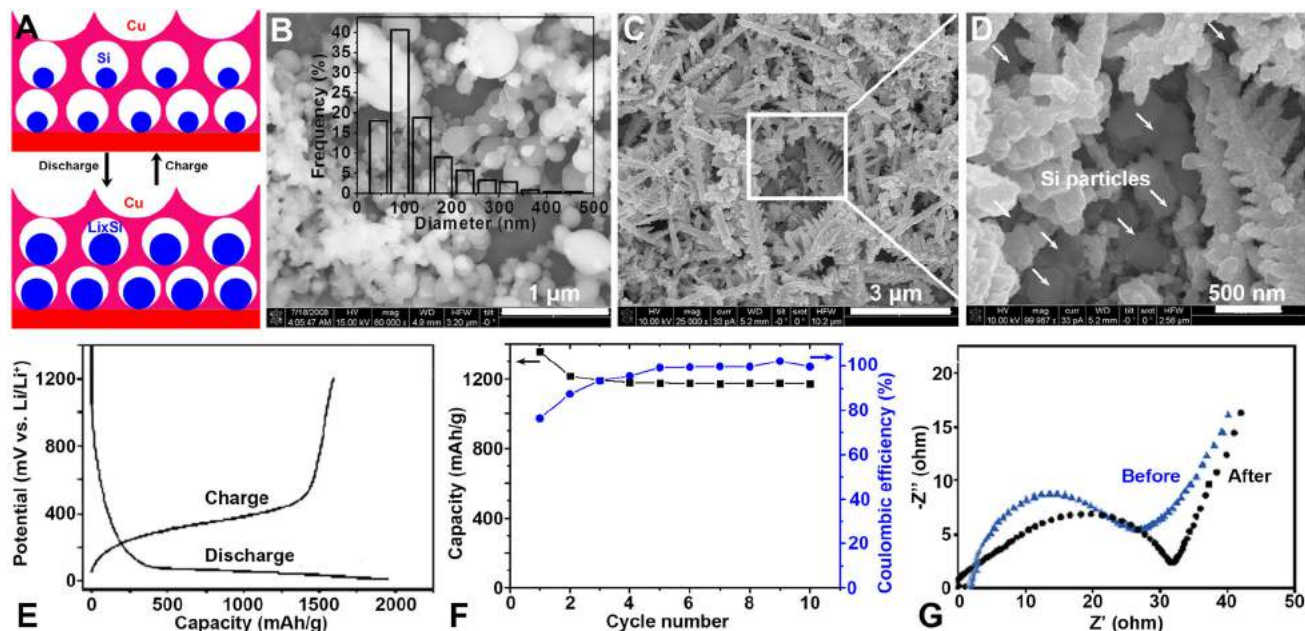

Fig. 10 Schematic description of a growth mechanism of electrical field-induced assembly of Cu NPs for 3D porous Cu structures

Fig. 11 (a) Schematic description of electrochemical cycling of Si particles in the porous Cu films, (b) SEM images and size distribution graph of the Si nanoparticles, and (c-d) SEM images, (e) charge–discharge curves at 0.1 C, (f) cycle performance at 1 C and (g) electrochemical impedance spectra of the porous Cu/Si composite films

The structure/morphology of the porous Cu materials could be tailored by varying the concentration of the additives, the applied potential/current densities and the assembly time. We also proposed a growth mechanism of the porous films for the field-induced assembly of Cu NPs or other NPs. Our study represents a facile and green way of creating 3D nanoporous structures that allow both fast transport of fluids and electron/ions and rapid electrochemical reactions due to the uniform but hierarchical nanostructures. Particularly, the porous Cu structures can function as electronic and mechanic substrates to capture active electrode materials for wide applications in lithium-ion batteries.

Acknowledgments

Conflict of Interest

The authors declare that they have no conflict of interest.

References

1. J. Park, S. Hyun, S. Suzuki, and H. Nakajima, Effect of Transference Velocity and Hydrogen Pressure on Porosity and Pore Morphology of Lotus-Type Porous Copper Fabricated by a Continuous Casting Technique, *Acta Mater.*, 2007, **55**, p 5646–5654

2. N. Wang, W.C. Hu, Y.H. Lu, Y.F. Deng, X.B. Wan, Y.W. Zhang, K. Du, and L. Zhang, Role of Surfactants in Construction of Porous Copper Film by Electrodeposition Approach, *Trans. IMF*, 2011, **89**, p 261–267

3. Y.-S. Choi, H.-R. Yu, and H.-W. Cheong, Electrochemical Properties of a Lithium-Impregnated Metal Foam Anode for Thermal Batteries, *J. Power Sources*, 2015, **276**, p 102–104

4. B.-T. Tsai, C.-J. Tseng, Z.-S. Liu, C.-H. Wang, C.-I. Lee, C.-C. Yang, and S.-K. Lo, Effects of Flow Field Design on the Performance of a PEM Fuel Cell with Metal Foam as the Flow Distributor, *Int. J. Hydrogen Energy*, 2012, **37**, p 13060–13066

5. C.-J. Tseng, B.T. Tsai, Z.-S. Liu, T.-C. Cheng, W.-C. Chang, and S.-K. Lo, A PEM Fuel Cell with Metal Foam as Flow Distributor, *Energy Convers. Manag.*, 2012, **62**, p 14–21

6. E. Bianchi, T. Heidig, C.G. Visconti, G. Groppi, H. Freund, and E. Tronconi, Heat Transfer Properties of Metal Foam Supports for Structured Catalysts: Wall Heat Transfer Coefficient, *Catal. Today*, 2013, **216**, p 121–134

7. N.D. Nikolić, G. Branković, and K.I. Popov, Optimization of Electrolytic Process of Formation of Open and Porous Copper Electrodes by the Pulsating Current (PC) Regime, *Mater. Chem. Phys.*, 2011, **125**, p 587–594

8. Y. Zhang, P. Zhu, L. Chen, G. Li, F. Zhou, D.D. Lu, R. Sun, F. Zhou, and C.-P. Wong, Hierarchical Architectures of Monodisperse Porous Cu Microspheres: Synthesis, Growth Mechanism, High-Efficiency and Recyclable Catalytic Performance, *J. Mater. Chem. A*, 2014, **2**, p 11966–11973

9. J. Ru, B. Kong, Y. Liu, X. Wang, T. Fan, and D. Zhang, Microstructure and Sound Absorption of Porous Copper Prepared by Resin Curing and Foaming Method, *Mater. Lett.*, 2015, **139**, p 318–321

10. L. Liu, J. Lyu, T. Zhao, and T. Li, Preparations and Properties of Porous Copper Materials for Lithium-Ion Battery Applications, *Chem. Eng. Commun.*, 2016, **203**, p 707–713

11. I. Najdovski and A.P. O'Mullane, The Effect of Electrode Material on the Electrochemical Formation of Porous Copper Surfaces Using Hydrogen Bubble Templating, *J. Electroanal. Chem.*, 2014, **722**, p 95–101

12. S. Hyun, K. Murakami, and H. Nakajima, Anisotropic Mechanical Properties of Porous Copper Fabricated by Unidirectional Solidification, *Mater. Sci. Eng., A*, 2001, **299**, p 241–248

13. S. Hyun and H. Nakajima, Effect of Solidification Velocity on Pore Morphology of Lotus-Type Porous Copper Fabricated by Unidirectional Solidification, *Mater. Lett.*, 2003, **57**, p 3149–3154

14. S.K. Hyun and H. Nakajima, Anisotropic Compressive Properties of Porous Copper Produced by Unidirectional Solidification, *Mater. Sci. Eng., A*, 2003, **340**, p 258–264

15. Y. Ahmed, M. Riad, A. Sayed, M. Ahlam, and M. Shalabi, Correlation Between Factors Controlling Preparation of Porous Copper via Sintering Technique Using Experimental Design, *Powder Technol.*, 2007, **175**, p 48–54

16. Y. Zhao, T. Fung, L. Zhang, and F. Zhang, Lost Carbonate Sintering Process for Manufacturing Metal Foams, *Scr. Mater.*, 2005, **52**, p 295–298

17. J. Hayes, A. Hodge, J. Biener, A. Hamza, and K. Sieradzki, Monolithic Nanoporous Copper by Dealloying Mn-Cu, *J. Mater. Res.*, 2006, **21**, p 2611–2616

18. Z. Dan, F. Qin, A. Makino, Y. Sugawara, I. Muto, and N. Hara, Fabrication of Nanoporous Copper by Dealloying Of Amorphous Ti-Cu-Ag Alloys, *J. Alloy. Compd.*, 2014, **586**, p S134–S138

19. T. Aburada, J.M. Fitz-Gerald, and J.R. Scully, Synthesis of Nanoporous Copper by Dealloying of Al-Cu-Mg Amorphous Alloys in Acidic Solution: The Effect of Nickel, *Corros. Sci.*, 2011, **53**, p 1627–1632

20. L.-J. Xue, Y.-F. Xu, L. Huang, F.-S. Ke, Y. He, Y.-X. Wang, G.-Z. Wei, J.-T. Li, and S.-G. Sun, Lithium Storage Performance and Interfacial Processes of Three Dimensional Porous Sn-Co Alloy Electrodes for Lithium-Ion Batteries, *Electrochim. Acta*, 2011, **56**, p 5979–5987

21. T. Jiang, S. Zhang, X. Qiu, M. Sun, and L. Chen, A Three-Dimensional Cellular Copper Prepared by Multiple-step Electrodeposition, *Electrochem. Solid-State Lett.*, 2008, **11**, p D50–D52

22. H.C. Shin, J. Dong, and M. Liu, Nanoporous Structures Prepared by an Electrochemical Deposition Process, *Adv. Mater.*, 2003, **15**, p 1610–1614

23. H.-C. Shin and M. Liu, Copper Foam Structures with Highly Porous Nanostructured Walls, *Chem. Mater.*, 2004, **16**, p 5460–5464

24. Y. Li, W.-Z. Jia, Y.-Y. Song, and X.-H. Xia, Superhydrophobicity of 3D Porous Copper Films Prepared Using the Hydrogen Bubble Dynamic Template, *Chem. Mater.*, 2007, **19**, p 5758–5764

25. P. Liu and K. Liang, Review Functional Materials of Porous Metals Made by P/M, Electroplating and Some Other Techniques, *J. Mater. Sci.*, 2001, **36**, p 5059–5072

26. L.H. Liu, J. Lyu, T.K. Zhao, and T.H. Li, Roles of Preparation Conditions in the Morphological Evolution of Electrodeposited Copper, *Dig. J. Nanomater. Biostruct.*, 2017, **12**, p 1021–1030

27. W.B. Liu, S.C. Zhang, N. Li, J.W. Zheng, and Y.L. Xing, A Facile One-Pot Route to Fabricate Nanoporous Copper with Controlled Hierarchical Pore Size Distributions Through Chemical Dealloying of Al-Cu Alloy in an Alkaline Solution, *Microporous Mesoporous Mater.*, 2011, **138**, p 1–7

28. T. Song, M. Yan, Z. Shi, A. Atrens, and M. Qian, Creation of Bimodal Porous Copper Materials by an Annealing-Electrochemical Dealloying Approach, *Electrochim. Acta*, 2015, **164**, p 288–296

29. K.T. Lee, J.C. Lytle, N.S. Ergang, S.M. Oh, and A. Stein, Synthesis and Rate Performance of Monolithic Macroporous Carbon Electrodes for Lithium-Ion Secondary Batteries, *Adv. Funct. Mater.*, 2005, **15**, p 547–556

30. L. Liu, B.G. Choi, S.O. Tung, T. Hu, Y. Liu, T. Li, T. Zhao, and N.A. Kotov, Low-Current Field-Assisted Assembly of Copper Nanoparticles for Current Collectors, *Faraday Discuss.*, 2015, **181**, p 383–401

31. L.H. Liu, J. Lyu, T.H. Li, and T.K. Zhao, Facile and Green Synthesis of Stable Aqueous Dispersions of Narrowly Distributed Copper Nanoparticles, *Dig. J. Nanomater. Biostruct.*, 2015, **10**, p 1303–1310

32. S.-H. Wu and D.-H. Chen, Synthesis of High-Concentration Cu Nanoparticles in Aqueous CTAB Solutions, *J. Colloid Interf. Sci.*, 2004, **273**, p 165–169

33. M. Singh, I. Sinha, M. Premkumar, A. Singh, and R. Mandal, Structural and Surface Plasmon Behavior of CU Nanoparticles Using Different Stabilizers, *Colloid. Surface. A*, 2010, **359**, p 88–94

34. P. Singh, A. Katyal, R. Kalra, and R. Chandra, Copper Nanoparticles in an Ionic Liquid: An Efficient Catalyst for the Synthesis of Bis-(4-hydroxy-2-oxothiazolyl) Methanes, *Tetrahedron Lett.*, 2008, **49**, p 727–730

35. X. Song, S. Sun, W. Zhang, and Z. Yin, A Method for the Synthesis of Spherical Copper Nanoparticles in the Organic Phase, *J. Colloid Interf. Sci.*, 2004, **273**, p 463–469

36. Y. Lee, J.-R. Choi, K.J. Lee, N.E. Stott, and D. Kim, Large-scale Synthesis of Copper Nanoparticles by Chemically Controlled Reduction for Applications of Inkjet-Printed Electronics, *Nanotechnology*, 2008, **19**, p 415604

37. H.-T. Zhu, C.-Y. Zhang, and Y.-S. Yin, Rapid Synthesis of Copper Nanoparticles by Sodium Hypophosphite Reduction in Ethylene Glycol Under Microwave Irradiation, *J. Cryst. Growth*, 2004, **270**, p 722–728

38. K.L. Tsai and J.L. Dye, Nanoscale Metal Particles by Homogeneous Reduction with Alkalides or Electrides, *J. Am. Chem. Soc.*, 1991, **113**, p 1650–1652

39. K.L. Tsai and J.L. Dye, Synthesis, Properties, and Characterization of Nanometer-Size Metal Particles by Homogeneous Reduction with Alkalides and Electrides in Aprotic Solvents, *Chem. Mater.*, 1993, **5**, p 540–546

40. R.M. Tilaki, A. Iraji zad, and S.M. Mahdavi, Size, Composition and Optical Properties of Copper Nanoparticles Prepared by Laser Ablation in Liquids, *Appl. Phys. A-Mater.*, 2007, **88**, p 415–419

41. H.-B. Lu, Y. Li, and F.-H. Wang, Synthesis of Porous Copper from Nanocrystalline Two-Phase Cu-Zr Film by Dealloying, *Scr. Mater.*, 2007, **56**, p 165–168

42. C. Wu, B. Mosher, and T. Zeng, One-Step Green Route to Narrowly Dispersed Copper Nanocrystals, *J. Nanopart. Res.*, 2006, **8**, p 965–969

43. H. Huang, F. Yan, Y. Kek, C. Chew, G. Xu, W. Ji, P. Oh, and S. Tang, Synthesis, Characterization, and Nonlinear Optical Properties of Copper Nanoparticles, *Langmuir*, 1997, **13**, p 172–175

44. Y. Wang and T. Asefa, Poly(allylamine)-stabilized Colloidal Copper Nanoparticles: Synthesis, Morphology, and Their Surface-Enhanced Raman Scattering Properties, *Langmuir*, 2010, **26**, p 7469–7474

45. Y.-F. Wang, Z.-M. Xiao, and C.-G. Zhang, Poly(allylamine)-stabilized Colloidal Copper Nanoparticles: Synthesis and Their SERS Activities, *Spectrosc. Spectr. Anal.*, 2012, **32**, p 1559–1561

46. Y. Kobayashi, S. Ishida, K. Ihara, Y. Yasuda, T. Morita, and S. Yamada, Synthesis of Metallic Copper Nanoparticles Coated with Polypyrrole, *Colloid Polym. Sci.*, 2009, **287**, p 877–880

47. X.-F. Tang, Z.-G. Yang, and W.-J. Wang, A Simple Way of Preparing High-Concentration and High-Purity Nano Copper Colloid for Conductive Ink in Inkjet Printing Technology, *Colloids Surfaces A*, 2010, **360**, p 99–104

48. W. Yu, H. Xie, L. Chen, Y. Li, and C. Zhang, Synthesis and Characterization of Monodispersed Copper Colloids in Polar Solvents, *Nanoscale Res. Lett.*, 2009, **4**, p 465–470

49. H.R. Ghorbani, Biological and Non-biological Methods for Fabrication of Copper Nanoparticles, *Chem. Eng. Commun.*, 2015, **202**, p 1463–1467

50. J.H. Kim, T.A. Germer, G.W. Mulholland, and S.H. Ehrman, Size-Monodisperse Metal Nanoparticles via Hydrogen-Free Spray Pyrolysis, *Adv. Mater.*, 2002, **14**, p 518–521

51. S. Shankar and J.-W. Rhim, Effect of Copper Salts and Reducing Agents on Characteristics and Antimicrobial Activity of Copper Nanoparticles, *Mater. Lett.*, 2014, **132**, p 307–311

52. X. Li, D. Zhu, and X. Wang, Evaluation on Dispersion Behavior of the Aqueous Copper Nano-Suspensions, *J. Colloid Interf. Sci.*, 2007, **310**, p 456–463

53. A. Yanase and H. Komiyama, In Situ Observation of Oxidation and Reduction of Small Supported Copper Particles Using Optical Absorption and X-ray Diffraction, *Surf. Sci.*, 1991, **248**, p 11–19

54. Y. Jian-Guang, Z. Yuang-Lin, T. Okamoto, R. Ichino, and M. Okido, A New Method for Preparing Hydrophobic Nano-Copper Powders, *J. Mater. Sci.*, 2007, **42**, p 7638–7642

55. J. Xiong, Y. Wang, Q. Xue, and X. Wu, Synthesis of Highly Stable Dispersions of Nanosized Copper Particles Using L-ascorbic Acid, *Green Chem.*, 2011, **13**, p 900–904

56. P. Kanninen, C. Johans, J. Merta, and K. Kontturi, Influence of Ligand Structure on the Stability and Oxidation of Copper Nanoparticles, *J. Colloid Interf. Sci.*, 2008, **318**, p 88–95

57. M. Samim, N.K. Kaushik, and A. Maitra, Effect of Size of Copper Nanoparticles on Its Catalytic Behaviour in Ullman Reaction, *Bull. Mater. Sci.*, 2007, **30**, p 535–540

58. S. Chen and J.M. Sommers, Alkanethiolate-Protected Copper Nanoparticles: Spectroscopy, Electrochemistry, and Solid-State Morphological Evolution, *J. Phys. Chem. B*, 2001, **105**, p 8816–8820

59. H.-C. Shin and M. Liu, Three-Dimensional Porous Copper-Tin Alloy Electrodes for Rechargeable Lithium Batteries, *Adv. Funct. Mater.*, 2005, **15**, p 582–586

60. Y. Li, Y.-Y. Song, C. Yang, and X.-H. Xia, Hydrogen Bubble Dynamic Template Synthesis of Porous Gold for Nonenzymatic Electrochemical Detection of Glucose, *Electrochem. Commun.*, 2007, **9**, p 981–988

61. J.-Y. Kim and N.A. Kotov, Charge Transport Dilemma of Solution-Processed Nanomaterials, *Chem. Mater.*, 2014, **26**, p 134–152

62. Z. Tang, N.A. Kotov, and M. Giersig, Spontaneous Organization of Single CdTe Nanoparticles into Luminescent Nanowires, *Science*, 2002, **297**, p 237–240

63. A. Querejeta-Fernández, J.C. Hernández-Garrido, H. Yang, Y. Zhou, A. Varela, M. Parras, J.J. Calvino-Gámez, J.M. González-Calbet, P.F. Green, and N.A. Kotov, Unknown Aspects of Self-Assembly of PbS Microscale Superstructures, *ACS Nano*, 2012, **6**, p 3800–3812

64. T. Hatchard and J. Dahn, In situ XRD and Electrochemical Study of the Reaction of Lithium with Amorphous Silicon, *J. Electrochem. Soc.*, 2004, **151**, p A838–A842

65. K. Peng, J. Jie, W. Zhang, and S.-T. Lee, Silicon Nanowires For Rechargeable Lithium-Ion Battery Anodes, *Appl. Phys. Lett.*, 2008, **93**, p 033105

66. C.K. Chan, H. Peng, G. Liu, K. McIlwrath, X.F. Zhang, R.A. Huggins, and Y. Cui, High-Performance Lithium Battery Anodes Using Silicon Nanowires, *Nat. Nanotechnol.*, 2007, **3**, p 31–35

67. K. Sawai, Y. Iwakoshi, and T. Ohzuku, Carbon Materials for Lithium-Ion (shuttlecock) Cells, *Solid State Ionics*, 1994, **69**, p 273–283

68. E. Yoo, J. Kim, E. Hosono, H.-S. Zhou, T. Kudo, and I. Honma, Large Reversible Li Storage of Graphene Nanosheet Families for Use in Rechargeable Lithium Ion Batteries, *Nano Lett.*, 2008, **8**, p 2277–2282

69. T.H. Hwang, Y.M. Lee, B.-S. Kong, J.-S. Seo, and J.W. Choi, Electrospun Core-Shell Fibers for Robust Silicon Nanoparticle-Based Lithium Ion Battery Anodes, *Nano Lett.*, 2012, **12**, p 802–807

70. H. Zhang and P.V. Braun, Three-Dimensional Metal Scaffold Supported Bicontinuous Silicon Battery Anodes, *Nano Lett.*, 2012, **12**, p 2778–2783

71. Y. Yu, L. Gu, C. Zhu, S. Tsukimoto, P.A. van Aken, and J. Maier, Reversible Storage of Lithium in Silver-Coated Three-Dimensional Macroporous Silicon, *Adv. Mater.*, 2010, **22**, p 2247–2250

72. L. Liu, J. Lyu, T. Li, and T. Zhao, Well-Constructed Silicon-Based Materials as High-Performance Lithium-Ion Battery Anodes, *Nanoscale*, 2016, **8**, p 701–722

73. L. Liu, F. Xie, J. Lyu, T. Zhao, T. Li, and B.G. Choi, Tin-Based Anode Materials with Well-Designed Architectures for Next-Generation Lithium-Ion Batteries, *J. Power Sources*, 2016, **321**, p 11–35